Layer 6 corticocortical neurons are a major route for intra and interhemispheric feedback

Simon Weiler[1], Manuel Teichert[2a] and Troy W. Margrie[1a*]

[1]Sainsbury Wellcome Centre for Neuronal Circuits and Behavior, University College London, 25 Howland Street, London W1T 4JG, United Kingdom

[2]Jena University Hospital, Department of Neurology, Am Klinikum 1, 07747 Jena, Germany

[a]M.T. and T.W.M. contributed equally to this work

*Corresponding author:

Name: Troy W. Margrie

Email address: t.margrie@ucl.ac.uk

Keywords: Cortical projectome, Interhemispheric, Layer 6, Anatomical hierarchy, Sensory-motor

Abstract

The mouse neocortex contains at least ninety distinctly defined yet interconnected areas that are symmetrically located across the two hemispheres. Determining the logic of this long range circuitry is necessary for understanding how inter-areal integration enables high level brain function involving multiple sensory, motor and cognitive processes. To address this we have performed a systematic anatomical analysis of the areal and laminar organization of the ipsilateral and contralateral cortical projection onto the primary visual (VISp), primary somatosensory barrel field (SSp-bfd) and primary motor (MOp) cortices. The resultant input maps reveal that although the ipsilateral hemisphere is the primary source of cortical input, there is substantial bilateral symmetry regarding the relative contribution and areal identity of contralateral input. Laminar analysis of these input areas show that excitatory Layer 6 corticocortical cells (L6 CCs) are a major projection pathway from both within and across the two hemispheres. Based on cortical hierarchy analysis that compares the relative contribution of inputs from supra- (feedforward) and infra-granular (feedback) layers, we find that contra-hemispheric projections reflect a dominant feedback organization compared to their ipsi-cortical counterpart. The magnitude of the interhemispheric difference in hierarchy was largest for sensory and motor projection areas compared to frontal, medial or lateral brain areas and can be explained by a proportional increase in input from L6 neurons. L6 CCs therefore not only mediate long-range cortical communication but also reflect its inherent feedback organization.

Introduction

The cortex is divided into two hemispheres that do not function independently. Rather, they are connected by commissural fibers, most notably the corpus callosum which is thought to coordinate function across the brain (Gazzaniga, 2000; Innocenti et al., 2022; Ocklenburg and Guo, 2024; Zhou et al., 2013). Within these circuits feedforward and feedback pathways represent two fundamental types of information flow (Berezovskii et al., 2011; Markov and Kennedy, 2013). In the case of sensory processing, feedforward connections typically carry sensory input towards areas higher in cortical hierarchy where more complex processing occurs (Felleman and Van Essen, 1991; Mumford, 1992; Rockland and Pandya, 1979; Siegle et al., 2021). Conversely, cortical feedback typically originates in higher-order areas and projects back to brain areas of lower hierarchical rank (Felleman and Van Essen, 1991; Markov et al., 2014; Rockland and Pandya, 1979). These pathways are believed to be crucial for modulating sensory processing (Weiler et al., 2024), enhancing signal fidelity (Xu et al., 2012), integrating contextual information (Zhang et al., 2014) and forming predictions (Keller and Mrsic-Flogel, 2018; Leinweber et al., 2017; Rao and Ballard, 1999).

Based on its cytoarchitecture the mammalian neocortex contains up to six layers that are believed to play distinct roles in feedforward and feedback processing (Harris et al., 2019; Markov et al., 2014, 2013). For instance, retrograde tracing (Markov et al., 2014) and physiological analysis (Bastos et al., 2015; Buffalo et al., 2011) in the visual cortical system of primates indicate that supragranular layers are the main source of feedforward projections while infragranular layers are the main source of feedback input. Moreover, the ratio of supra- to infra-granular layer projections has been used to reveal the anatomical basis of visual cortical hierarchy in primates and mice (Barone et al., 2000; D'Souza et al., 2022; Markov et al., 2014; Yao et al., 2023). While it is established that functional cortical hierarchy (at least in the visual system) reflects the laminar organization of cortical input within the ipsilateral hemisphere, it remains unknown how this is combined or even reflects the organization of input from the contralateral hemisphere. More specifically, to date there remains no cortex-wide anatomical analysis that investigates the nature of circuit hierarchy onto a given area that arises from both hemispheres. Also, which cortical layers are responsible for the establishment of the intra versus the interhemispheric cortical hierarchy is not understood.

In this study, we utilized state of the art retro-AAV based neuronal tracing in adult mice to determine the anatomical location of input neurons and map the cortex-wide projectome onto VISp, SSp-bfd and MOp. We employ an anatomically based hierarchy metric that not only enables us to define the contribution of Layer 2/3 (L2/3) and the infragranular layers but also

enables us to disassociate the roles of Layer 5 (L5) and L6 in the organization of cortical feedback circuits. Our results indicate extensive and symmetric projection patterns across the two hemispheres and reveal a key role for L6 in routing cortical feedback information.

Results

To systematically map the cortical projections onto primary sensory and motor cortical areas in adult mice, we utilized retrograde tracing with a recombinant AAV-variant, AAV-EF1a-H2B-EGFP (nuclear retro-AAV), which is taken up by axon terminals (Tervo et al., 2016) and results in EGFP expression in the nuclei of projection neurons (Fig.1A, Fig.S1A). This tracer was injected in either VISp (n = 6), SSp-bfd (n = 6), or MOp (n = 6), spanning across all cortical layers of each target area (Fig.1A, Fig.S2-S3). Importantly, only brains that had viral transduction levels of the white matter below 0.1% of the total bolus volume were included (Fig. S2B). Following ex-vivo two-photon tomography (Ragan et al., 2012) and 3D brain registration (Niedworok et al., 2016) detected cell nuclei (Tyson et al., 2021) were assigned according to the cortical areas of the Allen Mouse Brain Common Coordinate Framework ((Claudi et al., 2020; Wang et al., 2020), CCFv3, Fig.1B, excluding the targeted injection area). We found that the vast majority of neurons (>99%) projecting to all target areas were non-overlapping with GAD-expressing cells (Fig.S4A). Regarding L6 projection neurons, they were also found to be non-overlapping with NTSR1-expressing L6 corticothalamic cells and therefore indicative of L6 CCs (Fig.S4B,C).

The areal and modular organization of cortical input onto VISp, SSp-bfd and MOp

The resultant projection maps revealed labeling of several hundred thousand neurons located throughout both cortical hemispheres (Fig.S1B), with approximately 80% located ipsilaterally and 20% contralaterally (Fig.1B,C, $p<0.05$, two-sided Wilcoxon signed-rank test), irrespective of identity of the target injection site. While all three target areas received ipsilateral input from almost all cortical areas (VISp, range: 41 - 44, n = 6; SSp-bfd, range: 43 - 44, n = 6, MOp, range: 33 - 39, n = 6, Fig.1D) the two sensory cortical targets received input on average from more areas than the primary motor cortex (Fig.1D, sensory = 43.58 ± 0.26, n = 12 versus motor 36.67 ± 0.99, n = 6; $p < 0.001$, two-sided Wilcoxon rank-sum test). Comparing the inputs from both hemispheres showed that VISp and MOp injections revealed partial asymmetry in the number of areas labeled per hemisphere (Fig.1D, VISp ipsilateral = 43.33 ± 0.49 versus VISp contralateral 38.33 ± 0.72, MOp ipsilateral = 36.67 ± 0.99 versus MOp contralateral 30.67 ± 0.67, $p<0.05$, signed-rank test), whereas the source of input to SSp-bfd appeared to

be mirrored across the two hemispheres (Fig.1D, SSp-bfd ipsilateral = 43.83 ± 0.17 versus SSp-bfd contralateral 42 ± 1.61, p = 0.5, two-sided Wilcoxon signed-rank test).

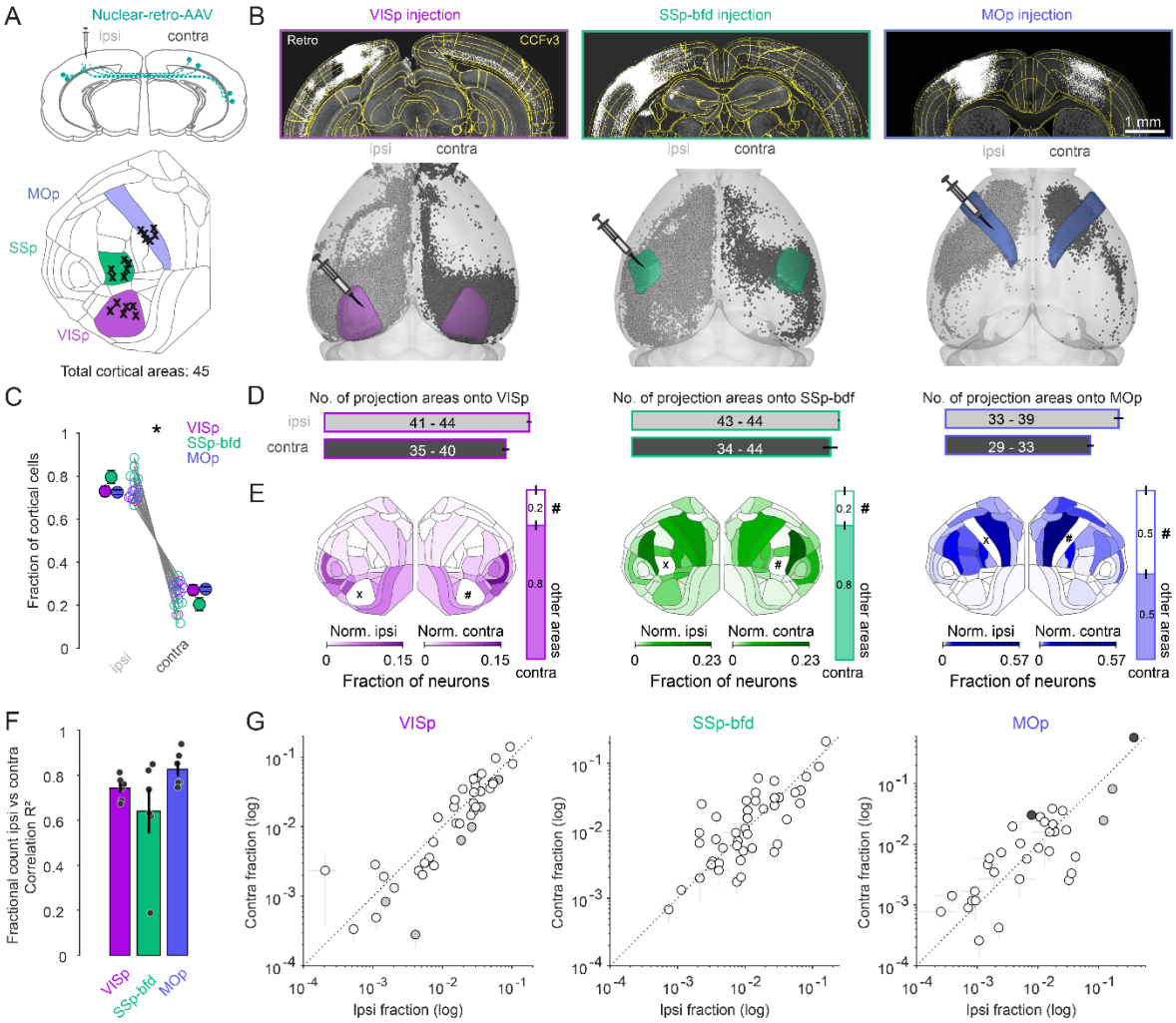

Figure 1: Widespread and bilaterally symmetrical cortical projections onto VISp, SSp-bfd and MOp. (A) Retrograde nuclear retro-AAV was injected across all layers of the primary visual cortex (VISp), somatosensory barrel field (SSp-bfd) and the motor cortex (MOp) of mice. The locations of the centroids on the injection bolus is shown on the CCFv3 cortical flat map. Injections performed in the right hemisphere injection (n = 11) are flipped to their corresponding location in the left hemisphere. (B) Two photon images showing examples of injection sites and labeled nuclei of retro-AAV labeled cells. Visualization of detected projection neurons for three individual mice warped into the 3D rendered space of the two hemispheres. (C) Plot showing the fraction of cortical cells per hemisphere detected for each mouse and pooled according to each injection site (mean ± sem). Asterisks indicate statistical significance ($p < 0.05$). (D) Bar graphs indicating the mean number (± sem) of cortical areas in which labeled neurons were observed. Text indicates the range of areas. (E) Flat maps indicating the relative cell counts normalized for each hemisphere excluding both the injection target (X) area its homotopic counterpart (#). Right, Bar graphs indicating the fraction of cells in the contralateral hemisphere located in the homotopic versus all other cortical areas (mean ± sem). Note that areas ILA (5), ENTl (44) and ENTm (45) are not represented in the cortical flat map on the left (see also Fig, S1C). (F) Bar graphs showing the average correlation (R^2 ± sem) of the ipsi- versus contra-lateral fractional count superimposed on the individual R^2 values for each experiment. (G) Plot of the ipsi- versus contra-lateral fractional count for each of the three target areas. Each circle represents the average of six fractional count values (± sem) for a given area. Open circles indicate instances where the difference of the ipsilateral values are not significant from the contralateral values. Black circles indicate a significant contralateral bias while gray circles indicate an ipsilateral bias. Dashed line indicates the unity line.

133
134 Importantly, we found there to be no instance where a projection area in the contralateral
135 hemisphere did not have an ipsilateral counterpart. These data show that both primary sensory
136 and motor cortices receive an abundance of functionally diverse input from cortical areas
137 outside their primary contralateral (homotopic) area indicating significant crossmodal
138 integration within and between the two hemispheres (Fig.1E).
139
140 To understand the relative contribution of a given area to the projectome for each hemisphere
141 we performed a correlation analysis on the relative fraction of labeled cells per area normalized
142 to the total hemispheric count. Excluding the homotopic target area, that always contained the
143 highest number of cells per area, but including all the cases where the number of cells in an
144 area exceed ten in at least three mice (see Methods), we found a strong correlation between
145 the fractional count of neurons in a given ipsilateral brain area with its contralateral counterpart
146 (VISp R^2 = 0.74 ± 0.02, $p<0.05$; SSp-bfd R^2 = 0.64 ± 0.1, $p<0.05$; MOp R^2 = 0.83 ± 0.03,
147 $p<0.05$, linear regression fit, Fig.1E,F). This relationship was observed independent of the
148 target identity (Fig.1F,G). When directly comparing the within hemisphere relative projection
149 weights of the individual cortical areas across the two hemispheres, we found that 33/40
150 (VISp), 44/44 (SSp-bfd) and 29/33 (MOp) were not significantly different from one another
151 which indicates significant bilateral symmetry in the relative contribution of a given area to its
152 hemispheric projectome (Fig.1G, individual one-sample t-tests on contra-ipsi difference,
153 Bonferroni multiple comparison correction).

154 Based on their degree of inter-areal cortical connectivity it has been suggested that the mouse
155 neocortex consists of six anatomical modules referred to as prefrontal, lateral, somatomotor,
156 visual, medial and auditory (Fig.2A, (Harris et al., 2019)). To determine whether the areal
157 projections reflect any underlying modular organization we next analyzed the distribution of
158 projection neurons according to their respective module. Firstly, while the VISp projection was
159 heavily dominated by input from the visual module (Fig.2B, ipsilateral visual module fractional
160 count 0.42 ± 0.02 versus lateral module 0.19 ± 0.02; contralateral visual module 0.42 ± 0.03
161 versus lateral module 0.22 ± 0.02, $p<0.001$, two-sided unpaired t-test), both the SSp-bfd and
162 MOp targets received input predominantly from the somatomotor module (Fig.2B, SSp-bfd:
163 ipsilateral somatomotor module fractional count 0.62 ± 0.05 vs. visual module 0.16 ± 0.03,
164 contralateral somatomotor module 0.53 ± 0.02 versus lateral module 0.24 ± 0.02, $p < 0.001$;
165 MOp: ipsilateral somatomotor module 0.83 ± 0.02 versus lateral module 0.08 ± 0.01,
166 contralateral somatomotor module 0.71 ± 0.03 versus lateral module 0.14 ± 0.01, $p < 0.001$,
167 two-sided unpaired t-test). For both the visual module projection to VISp and the somatomotor
168 module projections to SSp-bfd and MOp there were similar contributions from the majority of

the underlying areas (Fig.2C). Secondly, although both VISp and SSp-bfd received significant input from all modules in both hemispheres, we find there to be almost no input onto MOp from the visual, auditory and medial modules in either hemisphere (Fig.2B, less than 0.01 fractional count for each of these three modules). Finally, there also appears to be biases in the relative density of projections. For example, we find that the lateral module in the contralateral hemisphere projecting to VISp is more strongly weighted than its ipsilateral counterpart and that this is driven primarily by the connection from the temporal association area (TEa) and ectorhinal cortex (ECT) (Fig.2B,C, lateral module ipsilateral 0.19 ± 0.02 vs. contralateral 0.22 ± 0.02, $p = 0.05$, one-tailed paired t-test). While this contralateral dominance of the lateral module also emerges from the projection profiles to SSp-bfd and MOp it is rather mediated by many, albeit less dominant, lateral module areas (Fig.2C, SSp-bfd: lateral module fractional count ipsilateral 0.1 ± 0.01 versus contralateral 0.24 ± 0.02, $p<0.001$, one-tailed paired t-test, MOp: lateral module ipsilateral 0.08 ± 0.01 versus contralateral 0.14 ± 0.01, $p < 0.01$, one-tailed paired t-test).

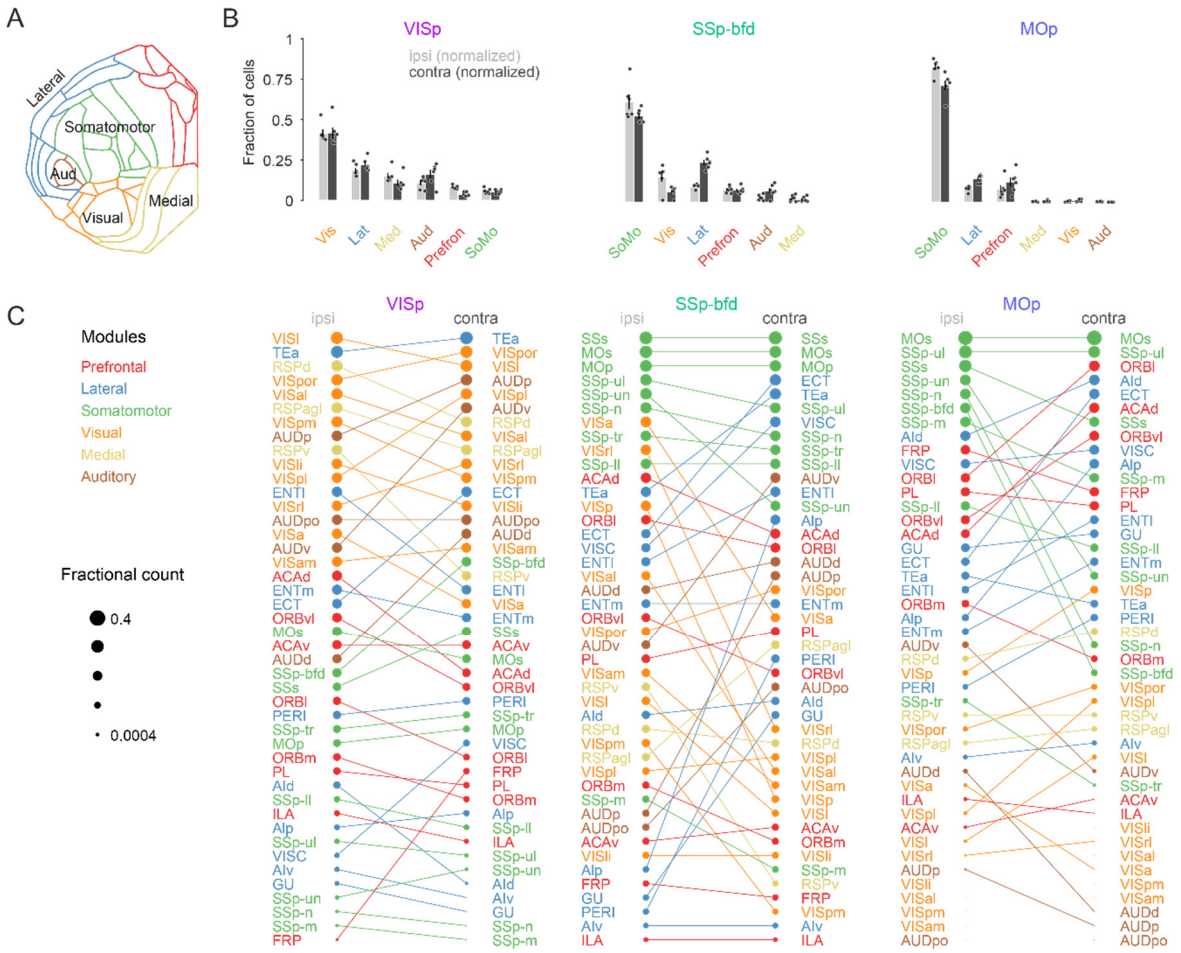

Figure 2: Modular organization of the intra and interhemispheric cortical projection onto VISp, SSp-bfd and MOp. (A) Schematic of the cortical flat map highlighting the six cortical modules and their corresponding areas. (B) Bar graphs of the normalized fractional cell counts for each of the six modules for ipsilateral and contralateral hemispheres ranked by decreasing ipsilateral weights. For the contralateral hemisphere the homotopic target region is not included. (C) Rank plot based on the relative weights of connectivity onto the target areas VISp, SSp-bfd and MOp for all cortical brain areas. The size of the circle indicates relative fractional count on a logarithmic scale. Corresponding areas on the ipsilateral and contralateral hemisphere are connected with a line.

The laminar organization of cortical input to VISp, SSp-bfd and MOp

Next, we asked whether there were specific subsets of projection neurons that might differentially contribute to the local and global projection by quantifying the distribution of neurons across all cortical layers in both hemispheres (Fig.3A1-A4). Firstly, for each injection target we find that the majority of detected neurons were located in L2/3, L5, and L6a (Fig.3B) with a very low fraction of labeled neurons in L4 and L6b. To begin to explore the laminar structure in the input to the three target areas we next compared the relative dominance of these three main layers. Regardless of hemisphere, L2/3 was found not to be the dominant layer of inter-areal input (Fig.3C1,C2,D1,D2). For VISp and MOp L6 dominated both the intra and interhemispheric projection (Fig.3C1,C2,D1,D2, $p<0.01$, one-way ANOVA, Tukey-Kramer multiple comparison correction). In the case of SSp-bfd L5 and L6 dominated the contralateral input (Fig.3C2,D2, L5 versus L2/3 and L6 versus L2/3, $p<0.01$, one-way ANOVA, Tukey-Kramer multiple comparison correction) and shared dominance with L2/3 only for the ipsilateral projection (Fig.3C1,D1, L5 versus L2/3, $p=0.06$; L6 versus L2/3, $p=0.64$, one-way ANOVA, Tukey-Kramer multiple comparison correction). When pooled across target areas, we find that the majority of projection source areas display L6 dominance, followed by L5 with only a small fraction of areas exhibiting L2/3 dominance (Fig.3E, $p < 0.05$, one-way ANOVA, Tukey-Kramer multiple comparison correction). These data show that L6 CCs are a key player mediating intra and interhemispheric connectivity onto primary sensory and motor areas.

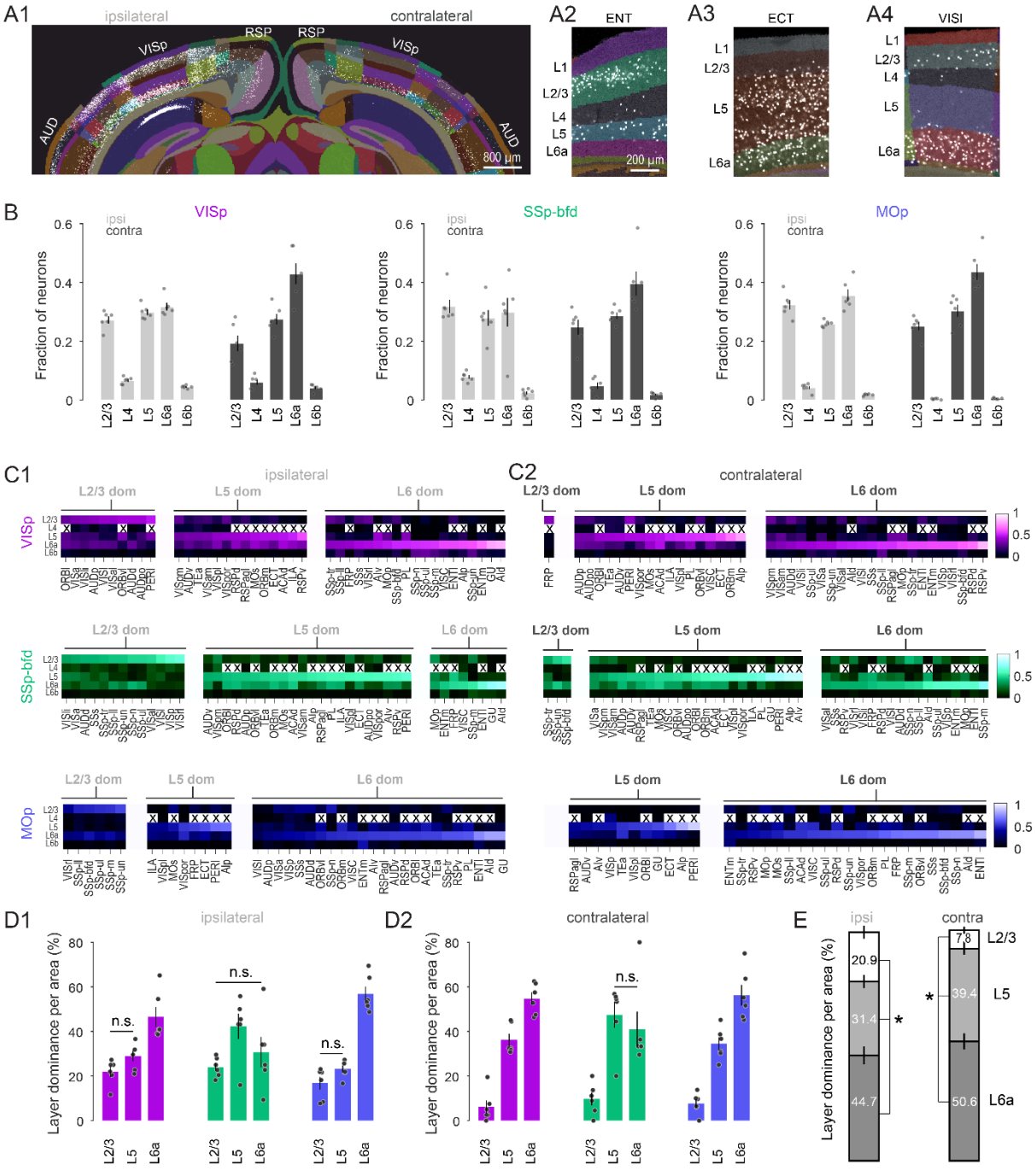

Figure 3: Cortical layer 6 is a major source of input to VISp, SSp-bfd and MOp. (A1) A segmented image of the cortex used to assign the laminar position of detected neurons after injection into VISp. Image of segmented Entorhinal (ENT), Ectorhinal (ECT), and lateral visual area (VISl) on the contralateral hemisphere showing local dominance by L2/3 (A2), L5 (A3) and L6a (A4), respectively. (B) Bar plot showing average fraction of cells (± sem, n = 6 mice) in L2/3, L4, L5, L6a and L6b across the ipsilateral and contralateral hemisphere for the three injection targets. (C) Average heat maps (n = 6 mice) based on the fractional count across laminae for each cortical area separated according to injection target and local dominance for ipsilateral (C1) and contralateral (C2) hemispheres. Dominance quantification is based on average laminar fractional count across animals. Crosses indicate cortical areas that do not contain L4. (D) Bar graphs showing the average percentage of areas (± sem, n = 6 mice) in which L2/3, L5 and L6 dominate the fractional cell count for ipsilateral (D1) and contralateral (D2) hemispheres. Unless indicated, all comparisons reach statistical significance (n.s. = non-significant). Dominance quantification is based on laminar fractional count per animal. (E) Stacked bar

227 plots showing average laminar dominance for all cortical areas (± sem) pooled across all injection
228 targets. Asterisks indicate statistical significance ($p < 0.05$).

229

230 Cortical input projections onto VISp, SSp-bfd and MOp reflect a hierarchical 231 organization

232

233 In primates, the laminar distribution of projection neurons has been used to interpret the
234 degree to which cortico-cortical networks might be feedforward or feedback (Barone et al.,
235 2000; Markov et al., 2014; Vezoli et al., 2021). A predominance of incoming projection neurons
236 from supragranular layers (L2/3) signifies a feedforward connection, whereas a higher
237 proportion in infragranular layers (layers 5 and 6) is considered to reflect a feedback projection
238 (Fig.4A). Additionally, cortical areas with a higher proportion of projection neurons in
239 infragranular, compared to supragranular layers, are suggested to have a higher hierarchical
240 rank (Fig.4A). Thus, the hierarchical rank of a specific projection area can be estimated by
241 calculating the fraction of infragranular labeled neurons (fILN) (Fig.4A,B). Previously in the
242 mouse visual cortex, similar anatomical measures of hierarchy have been performed using
243 anterograde tracers (D'Souza et al., 2022) and modified retrograde rabies virus (Yao et al.,
244 2023) to identify either target lamina or presynaptic cell populations. Using retrograde AAV-
245 EF1a-H2B-EGFP and by detecting EGFP expression in the nuclei of projection neurons we
246 find a very similar hierarchical ranking of the higher cortical visual areas as previously shown
247 (Fig.S5,(D'Souza et al., 2022; Siegle et al., 2021; Yao et al., 2023)).

248

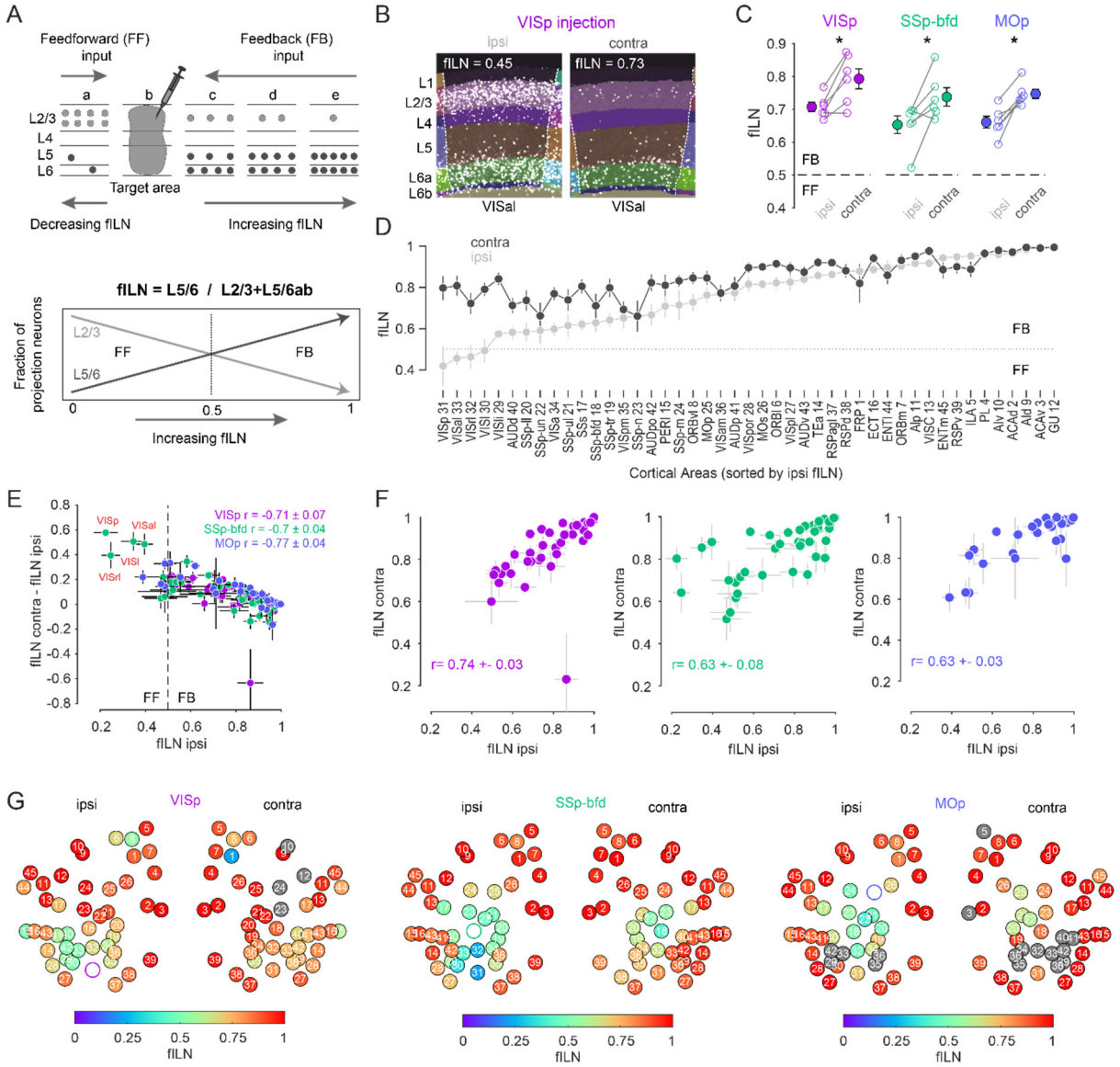

Figure 4: Cortical hierarchy onto VISp, SSp-bfd and MOp. (A) Cartoon showing the laminar basis of the anatomical determination of cortical hierarchy (Top). As the fraction of supragranular (L2/3) neurons decrease and/or the number of L5 and L6 neurons increase, the fraction of infragranular neurons (fILN) increases reflecting a predominance of feedback input (Bottom). (B) Segmented image of the ipsilateral and contralateral anterolateral visual area (VISal) projecting onto VISp showing the laminar position of detected cells. (C) Plots showing fILN values for all neurons within each hemisphere (blind to individual cortical areas) for each mouse for the three target injections. Average fILN values (± sem) are depicted by filled circles. (D) Plot showing the distribution of the average of ipsilateral fILN values (± sem) for n = 45 areas (pooled across different injection experiments) and ranked from lowest to highest (grey dots) The cortical areas abbreviations and their identification numbers are displayed at the bottom.Note: the number of data points contributing to each mean value ranges from 10 to 18 depending on the number of NaN values for a given area and whether it was excluded due to it being the target injection site. The average fILN values for the same but contralateral areas are also plotted according to their corresponding ipsilateral rank (black dots). (E) Scatter plot showing the correlation between the ipsilateral fILN values and the difference between the contralateral and ipsilateral fILN values for the three target injections. Average correlation values (± sem, n = 6 mice) for each target area are displayed (top right). Highlighted in red are the primary (VISp), rostrolateral (VISrl), lateral (VISl) and anterolateral (VISal) visual areas projecting to SSp-bfd that display low ipsilateral fILN and high contralateral fILN values. (F) Scatter plots showing the correlation between the ipsilateral and contralateral fILN values for the three target injections. Average correlation values (± sem, n = 6 mice) for each target area are displayed. (G) Heatmap plot displaying the ipsilateral and contralateral fILN values for each cortical

brain area for the three injection targets. Position of the circles correspond approximately to area location. Open circles denote injection areas. Gray circles indicate cortical areas where the number of cells projecting to VISp, SSp-bfd or MOp did not meet criterion. Numbers 1-45 indicate different brain areas, see also D.

Independent of the target area, the average fILN for both hemispheres indicates that cortical input onto VISp, SSp-bfd and MOp reflects predominantly a feedback organization (Fig.4C). However, on average, and compared to the ipsilateral projection, the average fILN of the contralateral hemisphere is larger across all injection targets (Fig.4C, $p < 0.05$, one-sided paired t-test, respectively). Moreover, the overall contralateral input appears more narrowly distributed in its degree of anatomical hierarchy, maintaining relatively high fILN values across all brain areas (Fig.4C,D; fILN range ipsilateral: 0.42 ± 0.1 - 1.0 ± 0.0 versus contralateral: 0.66 ± 0.07- 1 ± 0). As a consequence, regardless of the target area, we found a significant negative correlation between the areal fILN values on the ipsilateral side and the magnitude of the difference in the fILN of their contralateral counterpart (Fig.4E, VISp: r = -0.71 ± 0.07, SSp-bfd: r = -0.7 ± 0.04, MOp: r = -0.77 ± 0.04, $p<0.05$, Spearman correlation) although the ranking of contralateral hierarchy remained similar to that of the ipsilateral hierarchy (Fig4F, ipsilateral vs. contralateral fILN: VISp: r = 0.74 ± 0.03, SSp-bfd: r = 0.63 ± 0.08, MOp: r = 0.63 ± 0.03, $p<0.05$, Spearman correlation). In line with the classical view of reciprocal feedforward/feedback connectivity (Angelucci and Petreanu, 2023; Markov et al., 2014; Young et al., 2021) and in the case where we can directly compare the interconnectivity of two target sources within the ipsilateral hemisphere (VISp and SSp-bfd), we see feedforward input from VISp to SSp-bfd and feedback input from SSp-bfd to VISp (Fig.4E, Fig.S6A,B, magenta and green arrow). However, all contralateral areas were found to provide predominantly feedback input (Fig.4D-G Fig.S6A-C). These data also reveal unique instances, for example in SSp-bfd, where the ipsilateral and contralateral input from a subset of visual areas showed opposing signatures in their anatomical organization. Ipsilateral mediating feedforward while contralateral providing feedback input (highlighted in red in Fig.4E, Fig.S6A-C). Together, this hierarchical analysis shows that input onto these primary sensory and motor areas is mediated largely by a high proportion of L5 and L6 neurons and that both ipsilateral and contralateral input is predominantly feedback (Fig.4G). However, in some instances ipsilateral input can appear strongly feedforward and in stark contrast to the feedback organization of projections from the same area in the contralateral hemisphere.

Increased contralateral hierarchy is due to input from sensory and motor areas

Within the ipsilateral hemisphere, anterogradely labeled sensory-motor module projections have been shown to exhibit low hierarchy compared to lateral, medial and prefrontal modules (Harris et al., 2019). Using retrograde tracing and our fILN measure we find this to be the case

not only for the ipsilateral hemisphere but also for the contralateral hemisphere (Fig.5A). Strikingly, ranking cortical modules according to their fILN values revealed extremely similarly high levels of feedback from prefrontal, medial and lateral modules (pf-m-l) from both hemispheres. In contrast, the fILN values for visual, auditory and somatomotor (v-a-sm) modules were different across the two hemispheres (Fig.5A,B) with the contralateral hemisphere providing much stronger feedback (Fig.5A,B, ipsilateral fILN 0.65 ± 0.02 versus contralateral fILN 0.79 ± 0.01, $p < 0.001$, two-sided paired t-test). The difference between the ipsilateral and contralateral fILN was also significantly larger for the v-a-sm compared to the pf-m-l modules when the data was partitioned according to the target areas (Fig.5C, $p < 0.001$, one-sided paired t-test). This therefore appears to be another generalizable principle concerning the organizational hierarchy onto the primary sensory and motor cortices. Moreover, these results suggest that the global differences in the fILN between the two hemispheres observed above are mainly due to hemispheric differences in the fILN between the v-a-sm modules.

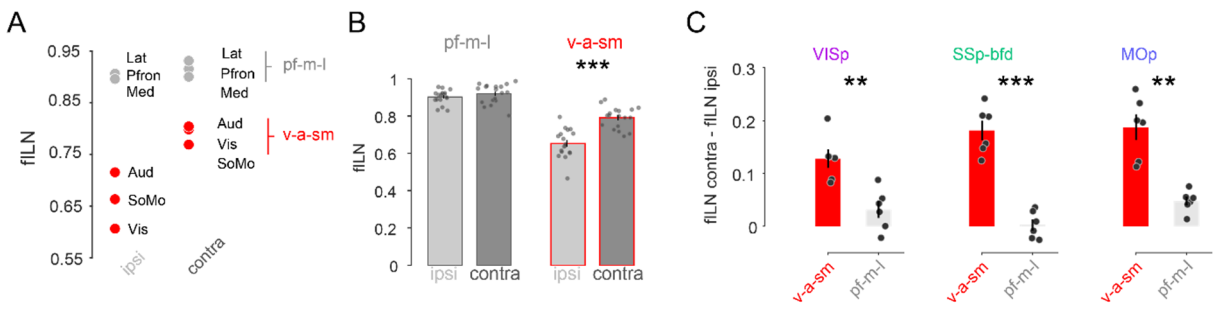

Figure 5: Sensory and motor but not lateral, prefrontal and medial projections explain the hemispheric differences in cortical hierarchy (A) Plot showing the average fILN values for all areas in a given module for n = 18 mice irrespective of target area. Red circles indicate the sensory and motor modules (visual, auditory and somatomotor; v-a-sm) while grey circles indicate prefrontal, medial and lateral (pf-m-l) modules. (B) Bar graphs comparing cross hemispheric fILN values (mean ± sem) for prefrontal, medial and lateral (pf-m-l) and sensory and motor (v-a-sm) modules. Each circle represents a single animal (n = 18). (C) Bar graphs (mean ± sem) showing the interhemispheric difference in fILN values between the two modular groupings for each target projectome. Each circle represents a single animal (n = 6, respectively).

L6 dominates the projection from many of the intra and interhemispheric cortical areas

We next sought to determine which cortical layers within the v-a-sm modules might account for the comparatively high contralateral fILN values. There are at least three possible scenarios that could give rise to high fILN values. Theoretically, increased fILN can stem from a reduction in the proportion of projection neurons located within L2/3, an increase in the proportion of projection neurons within L5/6, or a synergistic effect involving opposing changes in supra- and infra-granular layers (Fig.6A). By pooling all areas (n = 24) within the three key

341 sensory and motor modules for the contralateral side we observe a significant reduction in
342 L2/3 neurons for all target areas (Fig.6B, ipsilateral versus contralateral L2/3 fractional counts:
343 VISp 0.25 ± 0.02 versus 0.15 ± 0.02, SSp-bfd 0.36 ± 0.02 versus 0.22 ± 0.03, MOp 0.23 ±
344 0.01 versus 0.1 ± 0.01, $p<0.001$, one-sided paired t-test) and a concomitant increase in L6
345 cells in VISp and SSp-bfd (Fig.6B, ipsilateral versus contralateral L6 fractional counts: VISp
346 0.38 ± 0.02 versus 0.42 ± 0.01, SSp-bfd 0.24 ± 0.04 versus 0.4 ± 0.01, $p < 0.05$, one-sided
347 paired t-test). We found there to be no change in the fraction of L5 neurons between the
348 ipsilateral and contralateral hemispheres (Fig.6B, ipsilateral versus contralateral L5 fractional
349 counts: VISp 0.19 ± 0.02 versus 0.21 ± 0.01, $p = 0.38$; SSp-bfd 0.27 ± 0.04 versus 0.28 ± 0.01,
350 $p = 0.86$; MOp 0.13 ± 0.02 versus 0.12 ± 0.2, $p = 0.24$, two-sided paired t-test).
351
352 We next compared the fraction of projection neurons in a given layer to its counterpart area
353 and layer to identify which areal subpopulations of cells might be responsible for the observed
354 global differences in the fILN (Fig.6C). We find there to be many areas where the fraction of
355 L2/3 cells is significantly decreased compared to L5 and L6. L5 was more heterogeneous
356 containing instances of both decreases and increases in the average fraction of labeled cells
357 between the two hemispheres (Fig.6C). In the vast majority of cases L6 showed a relative
358 increase in its proportion of labelled cells compared to both L2/3 and L5. Taking only those
359 areas where we observed a significant change in the fraction of L2/3, L5 or L6 cells we found
360 that, depending on the target area, thirty to sixty percent of sensory-motor areas showed a
361 dramatic reduction in the fraction of contralaterally-labeled L2/3 neurons compared to their
362 ipsilateral areal counterparts. In contrast, between thirty to fifty percent of areas showed
363 increases in contralateral L6 cells. On the other hand, L5 showed on average little change
364 since its fractional contribution both increased and decreased depending on the target area
365 (Fig.6D). These data show that increased fILN in the contralateral hemisphere is due to an
366 increase in relative abundance of L6 CCs and indicates their key role in routing
367 interhemispheric feedback.
368
369 Finally, to determine the importance of L6 in the establishment of both the ipsilateral and
370 contralateral hierarchies and the difference between the two (Fig.4D), we excluded L6 from
371 the fILN calculation (Fig.4A). First, by comparing the default ipsilateral fILN values for all
372 cortical areas located within the v-a-sm modules to those when L5 or L6 was excluded, we
373 observe significant changes in fILN (Fig.6E, $p < 0.001$, two-sided paired t-test, Bonferroni
374 multiple comparison correction). Importantly, the reduction in ipsi fILN was greatest when L6
375 was excluded compared to L5 (Fig.6E, $p < 0.05$, one-sided paired t-test, Bonferroni multiple
376 comparison correction). This was also observed when performing the same comparisons on
377 the default contralateral fILN (Fig.6F). Excluding L6 from the contralateral default network

actually had such a significant impact that the resultant fILN was substantially lower than the default ipsilateral side (Fig.6F, default fILN ipsilateral 0.65 ± 0.03 vs. fILN contra excluding L6 0.52 ± 0.05, $p < 0.05$, one-sided paired t-test, Bonferroni multiple comparison correction). These data show that L6 exerts a major influence on the anatomical organization of cortical input onto VISp, SSp-bfd and MOp and accounts for the differences in the feedback hierarchy observed within and between the two hemispheres.

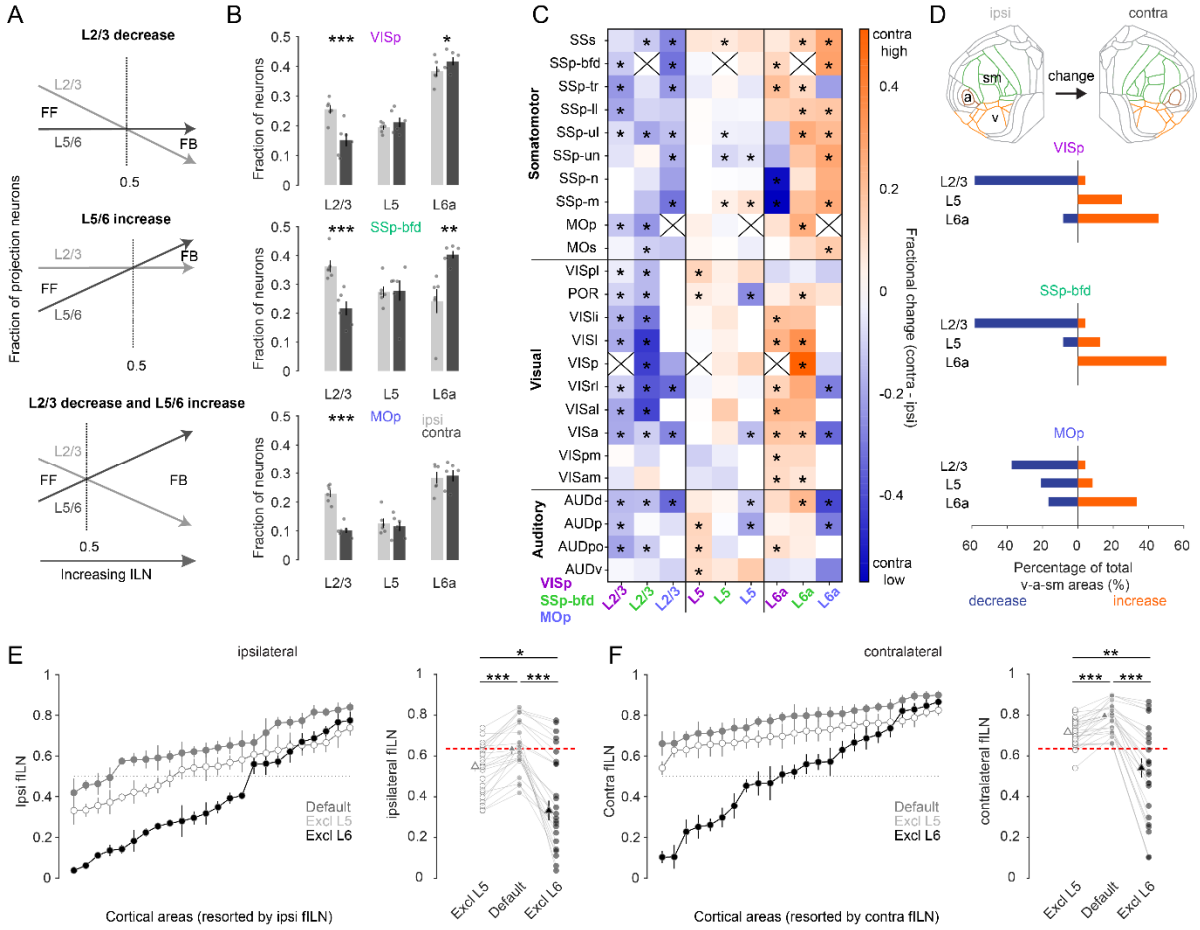

Figure 6: L6 dominates cortical hierarchy in the majority of sensory and motor areas. (A) Schematic illustrating at least three hypothetical ways in which changes in the relative distribution of L2/3, L5 and L6 neurons can give rise to increases in the fILN and reflect a predominantly feedback network. (B) Bar graphs showing the average (± sem) normalized fractional count (excluding L4 and 6b) of cells for the sensory and motor modules projecting to each target area from both hemispheres (ipsi, gray; contra, black), (C) Heat map displaying the fractional change of projections for L2/3, L5 and L6a between the contralateral and ipsilateral hemisphere. Displayed are the 24 individual brain areas in the sensory and motor modules for the three target areas VISp, SSp-bfd and MOp. Asterisks denote areas that significantly change between the ipsilateral and the contralateral hemispheres. Crosses indicate excluded homotopic areas. (D) Flat map indicating the three sensory and motor modules (top). Stacked horizontal bar plots displaying the percentage of the total number cortical areas in the sensory and motor modules that significantly decrease (blue) or increase (orange; indicated by the asterisks in C) for the three target areas. (E) (Left) Plots showing the average fILN (± sem) for each sensory and motor area (pooled across all target areas, n = 18 mice) and ranked according to the ipsilateral values for the default network (gray filled circles), the default network excluding L5 (open circles) and the default network excluding L6 (black filled circles). (Right) Scatter plots showing the average ipsilateral fILN scores for each of the twenty-four areas of the default network, the default network excluding L5

and the default network excluding L6. Filled triangles represent the mean (± sem) of the average fILN values. Red line indicates the mean of the ipsi default network. (F) (Left) Plots showing the average fILN (± sem) for each sensory and motor area (pooled across all target areas, n = 18 mice) and ranked according to the ipsilateral values for the default network (gray filled triangles), the contralateral values for the default network (gray filled circles), the contralateral values for the default network excluding L5 (open circles) and the default network excluding L6 (black filled circles). (Right) Scatter plots showing the average fILN scores for each of the twenty-four areas of the ipsi and contra default network, the default contra network excluding L5 and the default contra network excluding L6. Filled triangles represent the mean (± sem) of the average fILN values. Red line indicates the mean of the ipsi default network.

Discussion

By performing comprehensive bilateral cortical circuit mapping onto VISp, SSp-bfd and MOp we find that both primary sensory and motor areas receive extensive input from the majority of areas not only located in the ipsilateral (Ährlund-Richter et al., 2019; Brown et al., 2021; Hafner et al., 2019; Muñoz-Castañeda et al., 2021; Sun et al., 2019; Yao et al., 2023) but also contralateral cortical hemisphere (Goulas et al., 2017; Yao et al., 2023). This indicates significant cross-modal interactions not only within but also between the two cortical hemispheres. With only a few exceptions, we find that the identity, hierarchical rank and relative projection weights of input areas is highly conserved across the two hemispheres. One such exception relates to the contralateral lateral module whose composite cortical areas, compared to the ipsilateral module, display a stronger connection onto VISp, SSp-bfd and MOp indicating it may be a unique but generalisable feature of interhemispheric connectivity.

Earlier studies indicate that input from the other hemisphere onto a given area arises primarily and almost exclusively from the same contralateral area (Fenlon and Richards, 2015; Yorke and Caviness, 1975; Zhou et al., 2013). While we find many labeled cells in the contralateral target area, our data indicate that heterotopic connections are a prominent anatomical feature of the interhemispheric network (Goulas et al., 2017; Swanson et al., 2017; Szczupak et al., 2023; Yao et al., 2023). For both primary sensory areas, the majority of the contralateral input comes from heterotopic areas located within target areas' home module followed by areas located within most of the remaining modules. In contrast, MOp appears to receive very little input from areas relating to medial, visual and auditory modules.

Neurons projecting from the contralateral hemisphere are believed to primarily reside within L2/3 and to a lesser extent in L5 (Fame et al., 2011; Pal et al., 2024; Ramos et al., 2008; Yorke and Caviness, 1975). From an anatomical organization perspective, this would be designated as predominantly feedforward (Markov et al., 2014, 2013; Markov and Kennedy, 2013). We however find that L2/3 dominates the projection from the least number of cortical areas. Rather

441 for the majority of areas, L6 emerges as a major source of both the intra and especially the
442 interhemispheric projection (Liang et al., 2021; Olavarria and Van Sluyters, 1983; Yao et al.,
443 2023), especially for VISp and MOp. The combined dominance of L5 and L6 projecting
444 neurons shown here indicates that the vast majority of cortical projections to primary sensory
445 and motor regions are feedback in nature.
446
447 One explanation regarding the apparent discrepancy in these two sets of observations may
448 be due to technical differences and limitations of different tracing approaches. Chemical or
449 protein-based anterograde and retrograde tracers such as Cholera toxin subunit B (CTB) have
450 been widely used but have low transduction efficiency (Saleeba et al., 2019; Weiler et al.,
451 2024) compared to recently developed retrograde viruses (Tervo et al., 2016). Secondly,
452 mouse cre lines are a common tool for targeting specific cells in specific layers (Bortone et al.,
453 2014; Harris et al., 2019; Yao et al., 2023). However, as is the case for L6 CCs (Vélez-Fort et
454 al., 2014), not all cell types are accessible using cre-driver lines. In our study we targeted all
455 cell types located throughout all laminae within the target area that is in contrast to previous
456 tracing studies that appear biased towards upper layers of the injection area (Adaikkan et al.,
457 2022; Chovsepian et al., 2017; Massé et al., 2017). It also seems unlikely that the observed
458 predominance of L6 labelling revealed here can be attributed to labeling bias since our viral
459 injections effectively covered all cortical layers and excluded the white matter. Moreover,
460 multiple contralateral and ipsilateral areas exhibit significant labeling in L2/3 and/or 5 and prior
461 studies using non-viral tracers such as CTB or Fluorogold have similarly reported a dominance
462 of L6 projection neurons in the same specific pathways (e.g., SSp-bfd→ VISp, (Bieler et al.,
463 2017; Weiler et al., 2024)) as those revealed here using a retro-AAV based approach.
464
465 The idea that cortical feedforward and feedback circuits may have an anatomical signature
466 has been extensively interrogated in the mammalian visual cortical system (D'Souza et al.,
467 2022; Felleman and Van Essen, 1991; Harris et al., 2019; Markov et al., 2014; Yao et al.,
468 2023) where there exists a plethora of physiological data indicating functional hierarchy. In
469 primates, feedforward and feedback neurons tend to reside in different cortical layers (Markov
470 et al., 2014) and the ratio of supragranular to infragranular neurons has been employed to
471 anatomically define visual cortical hierarchy (P. Barone et al., 2000; Markov et al., 2014).
472
473 Here we demonstrate in mice that the fILN metric effectively ranks higher visual areas that is
474 consistent with the anatomical organization derived from axon termination patterns, as well as
475 retrograde rabies tracing (D'Souza et al., 2022; Harris et al., 2019; Yao et al., 2023) and
476 physiological experiments that describe functional hierarchy in mice (D'Souza et al., 2022; Jia
477 et al., 2022; Siegle et al., 2021). By applying fILN-based area ranking cortex-wide, we uncover

a global organization that is largely consistent with the hierarchical ranking of cortical areas based on anterograde labeling (Harris et al., 2019), placing sensory-motor modules at the bottom and lateral, medial and prefrontal modules at the top of cortical hierarchy. Our data therefore demonstrate that the fILN metric can serve as a continuous parameter whose ranking may be used as an estimate of feedforward and feedback hierarchy for understanding cortical connectivity.

Typically, feedforward projections are characterized as “drivers” while feedback projections are seen as “modulators” of neuronal activity (Markov et al., 2013). Our anatomical data reveal that VISp, SSp-bfd and MOp mostly receive feedback from the ipsilateral cortex. This is generally expected as these targets are the first cortical areas to receive sensory input or to initiate motor functions. The predominance of feedback projections suggests a modulatory role rather than driving input onto these primary cortical areas. From our data, the pairwise intra-hemispheric connectivity between VISp and SSp-bfd aligns well with historical theories of cortical hierarchy, which suggest that feedforward connections are typically complemented by reciprocal feedback connections, at least within the ipsilateral hemisphere (Angelucci and Petreanu, 2023; Felleman and Van Essen, 1991; Markov et al., 2013; Young et al., 2021). Our data also reveal a notable exception that appears to involve ipsilateral primary and higher visual cortical areas providing cross-modal feedforward input onto SSp-bfd. On the other hand, input from the same areas on the contralateral side are feedback in their organization as one might expect to observe for higher order areas. The fact that, regardless of the target area, contralateral projections are predominantly feedback suggests that the conventional rule of reciprocally feedforward and feedback projections does not apply for interhemispheric input at least to primary areas VISp, SSp-bfd or MOp. It will nevertheless be interesting and important to further investigate the hierarchical organization of cortical input onto higher cortical areas such anterior cingulate and retrosplenial cortex or within subregions of a given sensory area (e.g. higher compared to lower visual cortical areas).

Due to their dominant feedback bias, contralateral inputs may act as modulators of cortical activity within their ipsilateral target regions (Innocenti et al., 2022; Markov et al., 2014). For instance, inactivation of contralateral somatosensory areas in monkeys increases the receptive field size in the ipsilateral somatosensory area, suggesting a loss of modulatory contralateral input (Clarey et al., 1996). Moreover, contralateral auditory projections act to sharpen frequency tuning in its ipsilateral counterpart (Slater and Isaacson, 2020) and activation of contralateral visual projections strongly modulates visual cortical responses in the binocular zone of VISp (Zhao et al., 2013). However, these studies focused purely on homotopic areas while the functions of heterotopic areas largely remain elusive. Given the

observed extent of heterotopic input, future studies should address their functional roles in hemispheric communication and ultimately in behavior.

By showing that hierarchical disparities between the two hemispheres are largely accounted for by differences in the input from the sensory-motor modules, we offer a more nuanced understanding of interhemispheric communication and a prominent role for L6 that is strategically positioned within the cortex. Additionally, we show that increased fILN is predominantly due to the target areas receiving input from L6 CCs rather than L6 corticothalamic cells. L6 CCs not only integrate input from and output to its local cortical column (Vélez-Fort et al., 2014) but also receive substantial thalamic input, at least in sensory areas (Crandall et al., 2017). Moreover, responses of L6 CCs to external stimuli temporally precedes those in other cortical layers (Egger et al., 2020). Thus, L6 CCs are ideal candidates to rapidly relay information to other cortical areas thereby providing feedback modulation (Weiler et al., 2024), suggestive of predictive coding (Rao and Ballard, 1999) or the transmission of efference copy (Latash, 2021; Vallortigara, 2021; von Holst and Mittelstaedt, 1950).

References

Adaikkan C, Wang J, Abdelaal K, Middleton SJ, Bozzelli PL, Wickersham IR, McHugh TJ, Tsai L-H. 2022. Alterations in a cross-hemispheric circuit associates with novelty discrimination deficits in mouse models of neurodegeneration. *Neuron* **110**:3091-3105.e9. doi:10.1016/j.neuron.2022.07.023

Ährlund-Richter S, Xuan Y, van Lunteren JA, Kim H, Ortiz C, Pollak Dorocic I, Meletis K, Carlén M. 2019. A whole-brain atlas of monosynaptic input targeting four different cell types in the medial prefrontal cortex of the mouse. *Nat Neurosci* **22**:657–668. doi:10.1038/s41593-019-0354-y

Angelucci A, Petreanu L. 2023. Feedforward and Feedback Connections: Functional Connectivity, Synaptic Physiology, and Function In: Angelucci A, Usrey WM, Sherman SM, editors. The Cerebral Cortex and Thalamus. Oxford University Press. p. 0. doi:10.1093/med/9780197676158.003.0038

Barone, Batardiere A, Knoblauch K, Kennedy H. 2000. Laminar distribution of neurons in extrastriate areas projecting to visual areas V1 and V4 correlates with the hierarchical rank and indicates the operation of a distance rule. *J Neurosci Off J Soc Neurosci* **20**:3263–3281. doi:10.1523/JNEUROSCI.20-09-03263.2000

Bastos AM, Vezoli J, Bosman CA, Schoffelen J-M, Oostenveld R, Dowdall JR, De Weerd P, Kennedy H, Fries P. 2015. Visual areas exert feedforward and feedback influences through distinct frequency channels. *Neuron* **85**:390–401. doi:10.1016/j.neuron.2014.12.018

Berezovskii VK, Nassi JJ, Born RT. 2011. Segregation of feedforward and feedback projections in mouse visual cortex. *J Comp Neurol* **519**:3672–3683. doi:10.1002/cne.22675

Bieler M, Sieben K, Cichon N, Schildt S, Röder B, Hanganu-Opatz IL. 2017. Rate and Temporal Coding Convey Multisensory Information in Primary Sensory Cortices. *eNeuro* **4**. doi:10.1523/ENEURO.0037-17.2017

Bortone DS, Olsen SR, Scanziani M. 2014. Translaminar inhibitory cells recruited by layer 6 corticothalamic neurons suppress visual cortex. *Neuron* **82**:474–485. doi:10.1016/j.neuron.2014.02.021

Brown APY, Cossell L, Strom M, Tyson AL, Vélez-Fort M, Margrie TW. 2021. Analysis of segmentation ontology reveals the similarities and differences in connectivity onto L2/3 neurons in mouse V1. *Sci Rep* **11**:4983. doi:10.1038/s41598-021-82353-7

Buffalo EA, Fries P, Landman R, Buschman TJ, Desimone R. 2011. Laminar differences in gamma and alpha coherence in the ventral stream. *Proc Natl Acad Sci U S A* **108**:11262–11267. doi:10.1073/pnas.1011284108

Chovsepian A, Empl L, Correa D, Bareyre FM. 2017. Heterotopic Transcallosal Projections Are Present throughout the Mouse Cortex. *Front Cell Neurosci* **11**:36. doi:10.3389/fncel.2017.00036

Clarey JC, Tweedale R, Calford MB. 1996. Interhemispheric modulation of somatosensory receptive fields: evidence for plasticity in primary somatosensory cortex. *Cereb Cortex N Y N 1991* **6**:196–206. doi:10.1093/cercor/6.2.196

Claudi F, Petrucco L, Tyson AL, Branco T, Margrie TW, Portugues R. 2020. BrainGlobe Atlas API: a common interface for neuroanatomical atlases. *J Open Source Softw* **5**:2668. doi:10.21105/joss.02668

Claudi F, Tyson AL, Petrucco L, Margrie TW, Portugues R, Branco T. 2021. Visualizing anatomically registered data with brainrender. *eLife* **10**:e65751. doi:10.7554/eLife.65751

Crandall SR, Patrick SL, Cruikshank SJ, Connors BW. 2017. Infrabarrels Are Layer 6 Circuit Modules in the Barrel Cortex that Link Long-Range Inputs and Outputs. *Cell Rep* **21**:3065–3078. doi:10.1016/j.celrep.2017.11.049

D'Souza RD, Wang Q, Ji W, Meier AM, Kennedy H, Knoblauch K, Burkhalter A. 2022.

Hierarchical and nonhierarchical features of the mouse visual cortical network. *Nat Commun* **13**:503. doi:10.1038/s41467-022-28035-y

Egger R, Narayanan RT, Guest JM, Bast A, Udvary D, Messore LF, Das S, de Kock CPJ, Oberlaender M. 2020. Cortical Output Is Gated by Horizontally Projecting Neurons in the Deep Layers. *Neuron* **105**:122-137.e8. doi:10.1016/j.neuron.2019.10.011

Fame RM, MacDonald JL, Macklis JD. 2011. Development, specification, and diversity of callosal projection neurons. *Trends Neurosci* **34**:41–50. doi:10.1016/j.tins.2010.10.002

Felleman DJ, Van Essen DC. 1991. Distributed hierarchical processing in the primate cerebral cortex. *Cereb Cortex N Y N 1991* **1**:1–47. doi:10.1093/cercor/1.1.1-a

Fenlon LR, Richards LJ. 2015. Contralateral targeting of the corpus callosum in normal and pathological brain function. *Trends Neurosci* **38**:264–272. doi:10.1016/j.tins.2015.02.007

Gazzaniga MS. 2000. Cerebral specialization and interhemispheric communication: does the corpus callosum enable the human condition? *Brain J Neurol* **123 (Pt 7)**:1293–1326. doi:10.1093/brain/123.7.1293

Goulas A, Uylings HBM, Hilgetag CC. 2017. Principles of ipsilateral and contralateral cortico-cortical connectivity in the mouse. *Brain Struct Funct* **222**:1281–1295. doi:10.1007/s00429-016-1277-y

Hafner G, Witte M, Guy J, Subhashini N, Fenno LE, Ramakrishnan C, Kim YS, Deisseroth K, Callaway EM, Oberhuber M, Conzelmann K-K, Staiger JF. 2019. Mapping Brain-Wide Afferent Inputs of Parvalbumin-Expressing GABAergic Neurons in Barrel Cortex Reveals Local and Long-Range Circuit Motifs. *Cell Rep* **28**:3450-3461.e8. doi:10.1016/j.celrep.2019.08.064

Harris JA, Mihalas S, Hirokawa KE, Whitesell JD, Choi H, Bernard A, Bohn P, Caldejon S, Casal L, Cho A, Feiner A, Feng D, Gaudreault N, Gerfen CR, Graddis N, Groblewski PA, Henry AM, Ho A, Howard R, Knox JE, Kuan L, Kuang X, Lecoq J, Lesnar P, Li Y, Luviano J, McConoughey S, Mortrud MT, Naeemi M, Ng L, Oh SW, Ouellette B, Shen E, Sorensen SA, Wakeman W, Wang Q, Wang Y, Williford A, Phillips JW, Jones AR, Koch C, Zeng H. 2019. Hierarchical organization of cortical and thalamic connectivity. *Nature* **575**:195–202. doi:10.1038/s41586-019-1716-z

Innocenti GM, Schmidt K, Milleret C, Fabri M, Knyazeva MG, Battaglia-Mayer A, Aboitiz F, Ptito M, Caleo M, Marzi CA, Barakovic M, Lepore F, Caminiti R. 2022. The functional characterization of callosal connections. *Prog Neurobiol* **208**:102186. doi:10.1016/j.pneurobio.2021.102186

Jia X, Siegle JH, Durand S, Heller G, Ramirez TK, Koch C, Olsen SR. 2022. Multi-regional module-based signal transmission in mouse visual cortex. *Neuron* **110**:1585-1598.e9. doi:10.1016/j.neuron.2022.01.027

Keller GB, Mrsic-Flogel TD. 2018. Predictive Processing: A Canonical Cortical Computation. *Neuron* **100**:424–435. doi:10.1016/j.neuron.2018.10.003

Latash ML. 2021. Efference copy in kinesthetic perception: a copy of what is it? *J Neurophysiol* **125**:1079–1094. doi:10.1152/jn.00545.2020

Leinweber M, Ward DR, Sobczak JM, Attinger A, Keller GB. 2017. A Sensorimotor Circuit in Mouse Cortex for Visual Flow Predictions. *Neuron* **95**:1420-1432.e5. doi:10.1016/j.neuron.2017.08.036

Liang Y, Fan JL, Sun W, Lu R, Chen M, Ji N. 2021. A Distinct Population of L6 Neurons in Mouse V1 Mediate Cross-Callosal Communication. *Cereb Cortex N Y N 1991* **31**:4259–4273. doi:10.1093/cercor/bhab084

Markov NT, Ercsey-Ravasz M, Van Essen DC, Knoblauch K, Toroczkai Z, Kennedy H. 2013. Cortical high-density counterstream architectures. *Science* **342**:1238406. doi:10.1126/science.1238406

Markov NT, Kennedy H. 2013. The importance of being hierarchical. *Curr Opin Neurobiol* **23**:187–194. doi:10.1016/j.conb.2012.12.008

Markov NT, Vezoli J, Chameau P, Falchier A, Quilodran R, Huissoud C, Lamy C, Misery P, Giroud P, Ullman S, Barone P, Dehay C, Knoblauch K, Kennedy H. 2014a. Anatomy

of hierarchy: feedforward and feedback pathways in macaque visual cortex. *J Comp Neurol* **522**:225–259. doi:10.1002/cne.23458

Massé IO, Ross S, Bronchti G, Boire D. 2017. Asymmetric Direct Reciprocal Connections Between Primary Visual and Somatosensory Cortices of the Mouse. *Cereb Cortex N Y N 1991* **27**:4361–4378. doi:10.1093/cercor/bhw239

Mumford D. 1992. On the computational architecture of the neocortex. II. The role of cortico-cortical loops. *Biol Cybern* **66**:241–251. doi:10.1007/BF00198477

Muñoz-Castañeda R, Zingg B, Matho KS, Chen X, Wang Q, Foster NN, Li A, Narasimhan A, Hirokawa KE, Huo B, Bannerjee S, Korobkova L, Park CS, Park Y-G, Bienkowski MS, Chon U, Wheeler DW, Li Xiangning, Wang Yun, Naeemi M, Xie P, Liu L, Kelly K, An X, Attili SM, Bowman I, Bludova A, Cetin A, Ding L, Drewes R, D'Orazi F, Elowsky C, Fischer S, Galbavy W, Gao L, Gillis J, Groblewski PA, Gou L, Hahn JD, Hatfield JT, Hintiryan H, Huang JJ, Kondo H, Kuang X, Lesnar P, Li Xu, Li Y, Lin M, Lo D, Mizrachi J, Mok S, Nicovich PR, Palaniswamy R, Palmer J, Qi X, Shen E, Sun Y-C, Tao HW, Wakemen W, Wang Yimin, Yao S, Yuan J, Zhan H, Zhu M, Ng L, Zhang LI, Lim BK, Hawrylycz M, Gong H, Gee JC, Kim Y, Chung K, Yang XW, Peng H, Luo Q, Mitra PP, Zador AM, Zeng H, Ascoli GA, Josh Huang Z, Osten P, Harris JA, Dong H-W. 2021. Cellular anatomy of the mouse primary motor cortex. *Nature* **598**:159–166. doi:10.1038/s41586-021-03970-w

Niedworok CJ, Brown APY, Jorge Cardoso M, Osten P, Ourselin S, Modat M, Margrie TW. 2016. aMAP is a validated pipeline for registration and segmentation of high-resolution mouse brain data. *Nat Commun* **7**:11879. doi:10.1038/ncomms11879

Ocklenburg S, Guo ZV. 2024. Cross-hemispheric communication: Insights on lateralized brain functions. *Neuron* **112**:1222–1234. doi:10.1016/j.neuron.2024.02.010

Olavarria J, Van Sluyters RC. 1983. Widespread callosal connections in infragranular visual cortex of the rat. *Brain Res* **279**:233–237. doi:10.1016/0006-8993(83)90182-8

Osten P, Margrie TW. 2013. Mapping brain circuitry with a light microscope. *Nat Methods* **10**:515–523. doi:10.1038/nmeth.2477

Pal S, Lim JWC, Richards LJ. 2024. Diverse axonal morphologies of individual callosal projection neurons reveal new insights into brain connectivity. *Curr Opin Neurobiol* **84**:102837. doi:10.1016/j.conb.2023.102837

Ragan T, Kadiri LR, Venkataraju KU, Bahlmann K, Sutin J, Taranda J, Arganda-Carreras I, Kim Y, Seung HS, Osten P. 2012. Serial two-photon tomography for automated ex vivo mouse brain imaging. *Nat Methods* **9**:255–258. doi:10.1038/nmeth.1854

Ramos RL, Tam DM, Brumberg JC. 2008. Physiology and morphology of callosal projection neurons in mouse. *Neuroscience* **153**:654–663. doi:10.1016/j.neuroscience.2008.02.069

Rao RP, Ballard DH. 1999. Predictive coding in the visual cortex: a functional interpretation of some extra-classical receptive-field effects. *Nat Neurosci* **2**:79–87. doi:10.1038/4580

Rockland KS, Pandya DN. 1979. Laminar origins and terminations of cortical connections of the occipital lobe in the rhesus monkey. *Brain Res* **179**:3–20. doi:10.1016/0006-8993(79)90485-2

Saleeba C, Dempsey B, Le S, Goodchild A, McMullan S. 2019. A Student's Guide to Neural Circuit Tracing. *Front Neurosci* **13**:897. doi:10.3389/fnins.2019.00897

Siegle JH, Jia X, Durand S, Gale S, Bennett C, Graddis N, Heller G, Ramirez TK, Choi H, Luviano JA, Groblewski PA, Ahmed R, Arkhipov A, Bernard A, Billeh YN, Brown D, Buice MA, Cain N, Caldejon S, Casal L, Cho A, Chvilicek M, Cox TC, Dai K, Denman DJ, de Vries SEJ, Dietzman R, Esposito L, Farrell C, Feng D, Galbraith J, Garrett M, Gelfand EC, Hancock N, Harris JA, Howard R, Hu B, Hytnen R, Iyer R, Jessett E, Johnson K, Kato I, Kiggins J, Lambert S, Lecoq J, Ledochowitsch P, Lee JH, Leon A, Li Y, Liang E, Long F, Mace K, Melchior J, Millman D, Mollenkopf T, Nayan C, Ng L, Ngo K, Nguyen T, Nicovich PR, North K, Ocker GK, Ollerenshaw D, Oliver M, Pachitariu M, Perkins J, Reding M, Reid D, Robertson M, Ronellenfitch K, Seid S, Slaughterbeck C, Stoecklin M, Sullivan D, Sutton B, Swapp J, Thompson C, Turner

K, Wakeman W, Whitesell JD, Williams D, Williford A, Young R, Zeng H, Naylor S, Phillips JW, Reid RC, Mihalas S, Olsen SR, Koch C. 2021. Survey of spiking in the mouse visual system reveals functional hierarchy. *Nature* **592**:86–92. doi:10.1038/s41586-020-03171-x

Slater BJ, Isaacson JS. 2020. Interhemispheric Callosal Projections Sharpen Frequency Tuning and Enforce Response Fidelity in Primary Auditory Cortex. *eNeuro* **7**:ENEURO.0256-20.2020. doi:10.1523/ENEURO.0256-20.2020

Sun Q, Li X, Ren M, Zhao M, Zhong Q, Ren Y, Luo P, Ni H, Zhang X, Zhang C, Yuan J, Li A, Luo M, Gong H, Luo Q. 2019. A whole-brain map of long-range inputs to GABAergic interneurons in the mouse medial prefrontal cortex. *Nat Neurosci* **22**:1357–1370. doi:10.1038/s41593-019-0429-9

Swanson LW, Hahn JD, Sporns O. 2017. Organizing principles for the cerebral cortex network of commissural and association connections. *Proc Natl Acad Sci U S A* **114**:E9692–E9701. doi:10.1073/pnas.1712928114

Szczupak D, Iack PM, Rayêe D, Liu C, Lent R, Tovar-Moll F, Silva AC. 2023. The relevance of heterotopic callosal fibers to interhemispheric connectivity of the mammalian brain. *Cereb Cortex N Y N 1991* **33**:4752–4760. doi:10.1093/cercor/bhac377

Tervo DGR, Hwang B-Y, Viswanathan S, Gaj T, Lavzin M, Ritola KD, Lindo S, Michael S, Kuleshova E, Ojala D, Huang C-C, Gerfen CR, Schiller J, Dudman JT, Hantman AW, Looger LL, Schaffer DV, Karpova AY. 2016. A Designer AAV Variant Permits Efficient Retrograde Access to Projection Neurons. *Neuron* **92**:372–382. doi:10.1016/j.neuron.2016.09.021

Tyson AL, Rousseau CV, Niedworok CJ, Keshavarzi S, Tsitoura C, Cossell L, Strom M, Margrie TW. 2021. A deep learning algorithm for 3D cell detection in whole mouse brain image datasets. *PLoS Comput Biol* **17**:e1009074. doi:10.1371/journal.pcbi.1009074

Tyson AL, Vélez-Fort M, Rousseau CV, Cossell L, Tsitoura C, Lenzi SC, Obenhaus HA, Claudi F, Branco T, Margrie TW. 2022. Accurate determination of marker location within whole-brain microscopy images. *Sci Rep* **12**:867. doi:10.1038/s41598-021-04676-9

Vallortigara G. 2021. The Efference Copy Signal as a Key Mechanism for Consciousness. *Front Syst Neurosci* **15**:765646. doi:10.3389/fnsys.2021.765646

Vélez-Fort M, Rousseau CV, Niedworok CJ, Wickersham IR, Rancz EA, Brown APY, Strom M, Margrie TW. 2014. The stimulus selectivity and connectivity of layer six principal cells reveals cortical microcircuits underlying visual processing. *Neuron* **83**:1431–1443. doi:10.1016/j.neuron.2014.08.001

Vezoli J, Magrou L, Goebel R, Wang X-J, Knoblauch K, Vinck M, Kennedy H. 2021a. Cortical hierarchy, dual counterstream architecture and the importance of top-down generative networks. *NeuroImage* **225**:117479. doi:10.1016/j.neuroimage.2020.117479

von Holst E, Mittelstaedt H. 1950. Das Reafferenzprinzip. *Naturwissenschaften* **37**:464–476. doi:10.1007/BF00622503

Wang Q, Ding S-L, Li Y, Royall J, Feng D, Lesnar P, Graddis N, Naeemi M, Facer B, Ho A, Dolbeare T, Blanchard B, Dee N, Wakeman W, Hirokawa KE, Szafer A, Sunkin SM, Oh SW, Bernard A, Phillips JW, Hawrylycz M, Koch C, Zeng H, Harris JA, Ng L. 2020. The allen mouse brain common coordinate framework: a 3D reference atlas. *Cell* **181**:936-953.e20. doi:10.1016/j.cell.2020.04.007

Weiler S, Rahmati V, Isstas M, Wutke J, Stark AW, Franke C, Graf J, Geis C, Witte OW, Hübener M, Bolz J, Margrie TW, Holthoff K, Teichert M. 2024. A primary sensory cortical interareal feedforward inhibitory circuit for tacto-visual integration. *Nat Commun* **15**:3081. doi:10.1038/s41467-024-47459-2

Xu N, Harnett MT, Williams SR, Huber D, O'Connor DH, Svoboda K, Magee JC. 2012. Nonlinear dendritic integration of sensory and motor input during an active sensing task. *Nature* **492**:247–251. doi:10.1038/nature11601

Yao S, Wang Q, Hirokawa KE, Ouellette B, Ahmed R, Bomben J, Brouner K, Casal L,

Caldejon S, Cho A, Dotson NI, Daigle TL, Egdorf T, Enstrom R, Gary A, Gelfand E, Gorham M, Griffin F, Gu H, Hancock N, Howard R, Kuan L, Lambert S, Lee EK, Luviano J, Mace K, Maxwell M, Mortrud MT, Naeemi M, Nayan C, Ngo N-K, Nguyen T, North K, Ransford S, Ruiz A, Seid S, Swapp J, Taormina MJ, Wakeman W, Zhou T, Nicovich PR, Williford A, Potekhina L, McGraw M, Ng L, Groblewski PA, Tasic B, Mihalas S, Harris JA, Cetin A, Zeng H. 2023. A whole-brain monosynaptic input connectome to neuron classes in mouse visual cortex. *Nat Neurosci* **26**:350–364. doi:10.1038/s41593-022-01219-x

Yorke CH, Caviness VS. 1975. Interhemispheric neocortical connections of the corpus callosum in the normal mouse: a study based on anterograde and retrograde methods. *J Comp Neurol* **164**:233–245. doi:10.1002/cne.901640206

Young H, Belbut B, Baeta M, Petreanu L. 2021. Laminar-specific cortico-cortical loops in mouse visual cortex. *eLife* **10**:e59551. doi:10.7554/eLife.59551

Zhang S, Xu M, Kamigaki T, Do JPH, Chang W-C, Jenvay S, Miyamichi K, Luo L, Dan Y. 2014. Long-Range and Local Circuits for Top-Down Modulation of Visual Cortical Processing. *Science* **345**:660–665. doi:10.1126/science.1254126

Zhao X, Liu M, Cang J. 2013. Sublinear binocular integration preserves orientation selectivity in mouse visual cortex. *Nat Commun* **4**:2088. doi:10.1038/ncomms3088

Zhou J, Wen Y, She L, Sui Y-N, Liu L, Richards LJ, Poo M-M. 2013. Axon position within the corpus callosum determines contralateral cortical projection. *Proc Natl Acad Sci U S A* **110**:E2714-2723. doi:10.1073/pnas.1310233110

774 # Material and Methods

775 ## Animals

776 All experiments were performed on 6–23 week old mice. For the data presented in Figures 1-
777 6, 18 mice were used from which 11 were males and 7 were females. From these 18 mice 14
778 were wild type C57BL/6J mice, three were Gad2tm2(cre)Zjh/J (GAD-cre) and one mouse was
779 B6.FVB(Cg)-Tg(Ntsr1-cre)Gn220Gsat/Mmucd (Ntsr1-cre). The GAD-cre and NTSr1-cre mice
780 were crossed with B6.Cg-GT(ROSA)26 Sortm14(CAG-tdTomato)Hze/J (Ai14, Cre-dependent
781 tdTomato reporter) to achieve TdTomato reporter mice. Additionally, three Ntsr1-cre x Ai14
782 and three GAD-cre x Ai14 mice were used for the data presented in Fig.S4. Mice were raised
783 in standard cages on a 12 h light/dark cycle, with food and water available *ad libitum*. In this
784 study, 6 VISp-injected mice were previously used to quantify areal input from the ipsilateral
785 hemisphere (Weiler et al., 2024).
786 All surgeries and experiments were conducted in accordance with the UK Home Office
787 regulations (Animal (Scientific Procedures) Act 1986), approved by the Animal Welfare and
788 Ethical Review Body (AWERB; Sainsbury Wellcome Centre for Neural Circuits and Behavior)
789 and in compliance with ARRIVE guidelines. Every effort was made to minimize the number of
790 animals and their suffering.
791

792 ## Surgical procedures and viral injections

793 All surgical procedures were carried out under isoflurane (2%–5%) and after carprofen (5
794 mg/kg, s.c.) had been administered. For retrograde viral tracing, we used rAAV2-retro-EF1a-
795 H2B-EGFP (Nuclear retro-AAV, titer: 8.8 x 10^{13} GC per ml). Mice were anesthetized under
796 isoflurane (~2%) and craniotomies performed. Virus injection was performed using borosilicate
797 glass injection pipettes (Wiretrol II; Drummond Scientific) pulled to a taper length of ~30 mm
798 and a tip diameter of ~50 µm. Virus was delivered at a rate of 1–2 nl/s using Nanoject III
799 (Drummond Scientific, USA) and injected at three cortical depths covering all layers of the
800 VISp, SSp-bfd and MOp respectively (Fig.S3). After injections, the craniotomy was sealed with
801 silicon (kwik-cast), the skin was re-sutured and animals were allowed to recover for 2–4
802 weeks. Injection coordinates for the monocular and binocular zone of VISp, SSp-bfd and MOp
803 were based on the Allen Reference Atlas (coronal, 2D, (Wang et al., 2020).
804

805 ## Perfusion and brain extraction

806 For perfusions, mice were first deeply anesthetized using Pentobarbital Sodium (10 mg/kg). A
807 blunt needle was placed in the left ventricle, whilst an incision was performed in the right atrium
808 of the heart. Following this, blood was first cleared using 100 mM PBS. Subsequently, the
809 animal was perfused with saline containing 4% PFA. After successful fixation, the head was

810 removed and the brain dissected out. The brain was further fixed in 4% PFA overnight at 4 °C,
811 and then stored in 100 mM PBS at 4 °C until ready for imaging.
812

813 **Brain wide serial two-photon imaging**

814 For serial section two-photon imaging, on the day of imaging, brains were removed from the
815 PBS and dried. Brains were then embedded in agarose (4%) using a custom alignment mold
816 to ensure that the brain was perpendicular to the imaging axis. The agarose block containing
817 the brains were trimmed and then mounted onto the serial two photon microscope containing
818 an integrated vibrating microtome and motorized x–y–z stage (STP tomography, (Osten and
819 Margrie, 2013; Ragan et al., 2012)). For this, a custom system controlled by ScanImage (v5.6,
820 Vidrio Technologies, USA) using BakingTray (https://bakingtray.mouse.vision/) was used.
821 Imaging was performed using 920 nm illumination. Images were acquired with a 2.3 x 2.3 µm
822 pixel size, and 5 µm plane spacing. 8-10 optical planes were acquired over a depth of 50 µm
823 in total. To image the entire brain, images were acquired as tiles and then stitched using
824 StitchIt (https://doi.org/10.5281/zenodo.3941901). After each mosaic tile was imaged at all
825 optical planes, the microtome automatically cut a 50 µm slice, enabling imaging of the
826 subsequent portions of the sample and resulting in full 3D imaging of entire brains. All images
827 were saved as a series of 2D TIFF files.
828 Images were registered to the Allen Mouse Brain Common Coordinate Framework (Wang et
829 al., 2020) using the software brainreg (Tyson et al., 2022) based on the aMAP algorithm
830 (Niedworok et al., 2016). All atlas data were provided by the BrainGlobe Atlas API (Claudi et
831 al., 2020). For registration, the sample image data was initially down-sampled to the voxel
832 spacing of the atlas used and reoriented to align with the atlas orientation using bg-space
833 (https://doi.org/10.5281/zenodo.4552537). The 10 µm atlas was used for cell detection and
834 mapping. To manually segment viral injection sites, the software brainreg-segment (Tyson et
835 al., 2022) was used. Automated cell detection and deep learning based cell classification was
836 performed using the cellfinder software (Tyson et al., 2021) and cross-validated with manual
837 annotation (see validation in (Weiler et al., 2024)). All analysis in this manuscript was
838 performed in atlas space (Wang et al., 2020).
839 Figures showing detected cells in 3D atlas space were generated using the brainrender
840 software (Claudi et al., 2021) and custom scripts written in Python 3.9.
841

842 **Confocal imaging and analysis**

843 For a subset of Ntsr1-cre x Ai14 and GAD-cre x Ai14, slices cut with STP topography were
844 kept, post-fixed and mounted for confocal imaging (Leica SP8). Individual slices were imaged
845 using tile-scan acquisitions with a 10x air objective. Voxel sizes were 2 µm (x/y) and 3-6 µm

(z). We performed sequential imaging of GFP and td-tomato signals to achieve optimal spectral separation. We counted the overlap between GAD+ or NSTR1+ and retro-GFP+ cells using the Cell Counter feature of Fiji. Within the data set only approximately 1% of retro-GFP+ cells were GAD+ (Fig.S4) with no overlap between retro-GFP+ and NSTR1+ cells (Fig.S4).

Data analysis

Cellfinder outputs a CSV file containing the laminar count of detected nuclei for each cortical area. This was analyzed using custom-written code in MATLAB 2023-24 and Python 3.9. We applied the following criteria for data exclusion: 1) Instances where more than 30% of the viral injection bolus was located outside the respective target area (VISp, SSp-bfd or MOp, Fig. S2A-D). 2) A given cortical area in a given hemisphere had to contain 10 or more cells. In the case where a given area contained less than 10 cells the area cell was set at zero. 3) Additionally to be included in the analysis a given area had to contain more than 10 cells in at least three injections and in the same hemisphere of three different mice. For comparison of the laminar distribution of cells within different brain areas, values were normalized to the total number of cells detected in each area. The fILN was calculated as following:

$$fILN = \left(L5_{fraction\ area} + L6_{fraction\ area}\right) / \left(L2/3_{fraction\ area} + L5_{fraction\ area} + L6_{fraction\ area}\right).$$

Statistics

Details of all n numbers and statistical analysis are provided either in the results and/or in the figure captions. Before comparison of data, individual data sets were checked for normality using the Anderson-Darling test in MATLAB 2023-24. The required sample sizes were estimated based on literature and our past experience performing similar experiments (Brown et al., 2021; Weiler et al., 2024). Significance level was typically set as $p<0.05$ if not stated otherwise. Statistical analyses were performed using MATLAB 2023-24. Asterisks indicate significance values as follows: *$p < 0.05$, **$p < 0.01$, ***$p < 0.001$.

Data, Materials, and Software Availability

Analysis code and structure of processed data has been deposited on GitHub: https://github.com/simonweiler/serial2p. Raw data are available on request.

Acknowledgements

We thank Panagiota Iordanidou for excellent technical support and assistance as well as Mateo Vélez-Fort for comments on the manuscript. The authors are further grateful to the support staff of the Neurobiological Research Facility at Sainsbury Wellcome Centre. T.W.M. and S.W. are funded by The Wellcome Trust (214333/Z/18/Z; 090843/F/09/Z) and Humboldt Foundation (S.W.). M.T. is funded by the Interdisciplinary Centre for Clinical Research (IZKF; Advance medical scientist - Program 11).

Author contributions

S.W., M.T. and T.W.M conceived the project. S.W. performed all tracing and imaging experiments. S.W. and M.T. analyzed all data. M.T., T.W.M and S.W. interpreted and discussed all data and wrote the manuscript.

Competing interests

The authors declare no competing interest.